

Ho Lee*

e-mail: hlee14@partners.org
Dept. of Mechanical Engineering,
The University of Texas at Austin,
Texas Longhorns, Austin, TX 78712,
Phone: (512) 471-9497,
Fax: (512) 232-4919
Wellman Laboratories of Photomedicine
Massachusetts General Hospital, BHX 630
Harvard Medical School,
50 Blossom Street, Boston, MA, 02114,
Phone: (617) 724-2067,
Fax: (617) 724-2075

Robert T. Ryan

e-mail: urobros@msn.com
Divisions of Urology,
University of Texas Health Science Center,
7703 Floyd Curl Drive,
San Antonio, TX 78229,
Phone: (210) 567-5640,
Fax: (210) 567-6868

Jeehyun Kim

e-mail: jeehyun@mail.utexas.edu
Dept. of Biomedical Engineering,
The University of Texas at Austin,
Texas Longhorns, Austin, TX 78712,
Phone: (512) 471-9497,
Fax: (512) 232-4919

Bernard Choi

e-mail: bchoi@laser.blii.uci.edu
Bechman Laser Institute and Medical Clinic,
University of California,
1002 Health Sciences Road East,
Irvine, CA 92612,
Phone: (949) 824-3754,
Fax: (949) 824-6969

Navanit V. Arakeri

e-mail: navanit_a@hotmail.com
Dept. of Biomedical Engineering,
The University of Texas at Austin,
Texas Longhorns, Austin, TX 78712,
Phone: (512) 471-9497,
Fax: (512) 232-4919

Joel M. H. Teichman

e-mail: teichman@uthscsa.edu
Divisions of Urology,
University of Texas Health Science Center,
7703 Floyd Curl Drive,
San Antonio, TX 78229,
Phone: (210) 567-5640,
Fax: (210) 567-6868

A. J. Welch

e-mail: welch@mail.utexas.edu
Dept. of Biomedical Engineering,
The University of Texas at Austin,
Texas Longhorns, Austin, TX 78712,
Phone: (512) 471-9497,
Fax: (512) 232-4919

Dependence of Calculus Retropulsion Dynamics on Fiber Size and Radiant Exposure During Ho:YAG Lithotripsy

During pulsed laser lithotripsy, the calculus is subject to a strong recoil momentum which moves the calculus away from laser delivery and prolongs the operation. This study was designed to quantify the recoil momentum during Ho:YAG laser lithotripsy. The correlation among crater shape, debris trajectory, laser-induced bubble and recoil momentum was investigated. Calculus phantoms made from plaster of Paris were ablated with free running Ho:YAG lasers. The dynamics of recoil action of a calculus phantom was monitored by a high-speed video camera and the laser ablation craters were examined with Optical Coherent Tomography (OCT). Higher radiant exposure resulted in larger ablation volume (mass) which increased the recoil momentum. Smaller fibers produced narrow craters with a steep contoured geometry and decreased recoil momentum compared to larger fibers. In the presence of water, recoil motion of the phantom deviated from that of phantom in air. Under certain conditions, we observed the phantom rocking towards the fiber after the laser pulse. The shape of the crater is one of the major contributing factors to the diminished recoil momentum of smaller fibers. The re-entrance flow of water induced by the bubble collapse is considered to be the cause of the rocking of the phantom. [DOI: 10.1115/1.1786297]

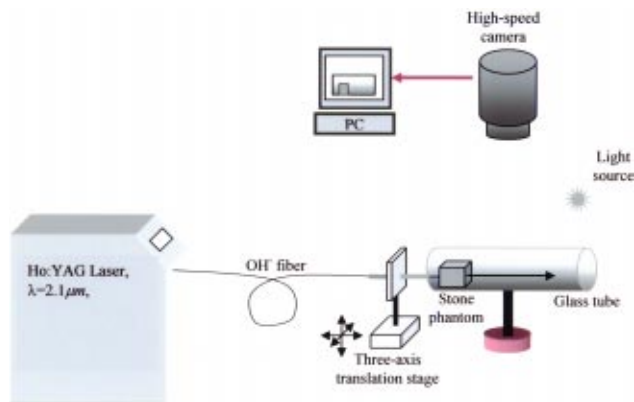


Fig. 1 Experimental setup used to measure the initial velocity of the calculus phantom after the laser pulse

Introduction

Previous reports have demonstrated the clinical feasibility of fragmenting urinary and biliary calculi with high power lasers [1,2]. Several pulsed lasers such as pulsed dye, alexandrite, and Ho:YAG have been successfully used as intracorporeal lithotriptors [3–5]. Calculus fragmentation for short pulse lasers (pulse duration less than 1 μ s) is mainly produced by the combination of laser energy absorption and resultant laser-induced shock wave, whereas long pulse Ho:YAG lithotripsy is considered a thermal process [5–7]. During pulsed laser calculus interaction, the calculus is subject to a strong recoil momentum caused by the combined effect of the fragmented particle ejection, bubble expansion and collapse, and the laser induced shock wave [8–19]. This momentum may cause the calculus to recoil away from the laser delivery fiber; the physician then must move the fiber to the new calculus position for additional laser irradiation. This cumbersome process makes the procedure inconvenient and difficult, and eventually prolongs the operation.

This study was designed to quantify the recoil momentum during the Ho:YAG laser lithotripsy. The dynamics of recoil action of a calculus phantom was monitored with a high-speed video camera and ablation craters were examined with Optical Coherent Tomography (OCT) [20–21]. The trajectory of ejected debris was studied also. The correlation among crater shape, debris trajectory, laser-induced bubble and recoil momentum was investigated.

Materials and Methods

Calculus phantoms with a mass of 150 mg and a dimension of 5 mm³ were made from plaster of Paris (calcium phosphate). The calculus phantom was placed in a model of the ureter (Fig. 1) consisting of a clear glass tube with an inner diameter of 12.5 mm and a length of 15 cm. Both ends of the tube were sealed with polymer clay. The experiment was performed with and without deionized water in the tube. A clinical Ho:YAG laser (VersaPulse Select, Lumenis, CA) and a scientific Ho:YAG laser (1-2-3 laser, Schwartz Electro Optics, FL) were employed in our study. Both lasers emit 2.1 μ m laser pulses with a pulse duration of 250 ~ 300 μ sec. A Ho:YAG pulse was delivered to a calculus phantom via low OH⁻ quartz fibers (SlimLine™ 200, 365, 550 and 1000, Lumenis, CA) inserted into the tube through a small hole of the sealing polymer clay. Before each irradiation, the fiber was placed in contact with the phantom and the irradiation spot was adjusted with a three-axis translation stage to be centered on the phantom. Before and after the ablation, the laser energy out of the

*Current mailing address: Wellman Laboratories of Photomedicine Massachusetts General Hospital, BHX 630 Harvard Medical School, 50 Blossom Street, Boston, MA, 02114, Phone: (617) 724-2067, Fax: (617) 724-2075.

distal end of the fiber was measured with an energy meter (EPM 2000, Molectron, OR) equipped with a pyroelectric joulemeter (J25, Molectron, OR). To eliminate potential artifacts due to fiber damage during laser irradiation, measurements were considered valid only if the transmission loss after irradiation was less than 10% of input laser energy.

Motion of the calculus phantom was monitored with a high-speed video camera (FASTCAM Super 3K, Photron, CA) that allowed us to take pictures at 1000 frames per second. A white light source illuminated the glass tube and phantom. The high-speed video camera and lens system were adjusted to capture the motion of the phantom with a spatial resolution of 3 μ m. Acquired images were transferred to a PC equipped with a frame grabber. Edges of the transferred digital images were enhanced using *Image Processing toolbox* in *Matlab* (The Mathworks, MA).

A series of experiments was conducted to measure the initial velocity of the phantom after the pulse under various conditions. Variables included laser energy (200, 400, 500, 800 and 1000 mJ) and fiber diameter (272, 365, 550 and 940 μ m). The laser-induced repulsive force was assumed as an impulse impact due to its short existence (less than 1 msec). The initial displacement (the displacement during the first millisecond after the onset of the laser pulse) of the repulsion phantom was measured by examining the first two frames after the laser pulse. The initial velocity of the phantom was calculated from the initial displacement and travel time (1 msec). The linear recoil momentum was determined from the product of mass and initial velocity.

$$J_{rm} = m_{rm} v_{rm} \quad (1)$$

where J_{rm} = linear recoil momentum (kg \times m/sec), m_{rm} = mass of phantom (kg), and v_{rm} = initial velocity of phantom (m/sec). The effect of friction and drag force during the first millisecond was assumed to be negligible

Laser induced craters were examined with an OCT system ($\lambda_0 = 1290$ nm and $\Delta\lambda = 42$ nm) with a lateral and axial resolution of ~ 20 μ m to obtain the quantitative ablation crater shape [22]. A series of cross sectional images was obtained over the entire crater, with a 40 μ m distance between each image. Ablation volume was estimated from OCT cross-sections over the crater volume.

The propagation direction of the laser-induced ablation plume governs the direction and magnitude of recoil momentum [8–14]. To investigate the direction of plume propagation after being ablated, we used the high-speed video camera to monitor the dynamics of the laser-induced plume [23]. Laser burn paper (Kentek, NH) was placed 2 cm away from the fiber at three different angles with respect to the fiber (perpendicular and ± 45 deg) and then irradiated with a single Ho:YAG laser pulse (940 μ m fiber and 500 mJ of pulse energy). The trajectory of the ejected ablation plume was determined from the acquired image sequences.

Results

Recoil Action of Calculus Phantom During Pulsed Laser Lithotripsy. The laser-induced plume and recoil action of the phantom can be observed in consecutive pictures presented in Fig. 2. For illustration purpose, in this example, the phantom was placed on a metal surface to demonstrate the process. The actual recoil momentum data presented below were obtained with phantoms in a glass tube. The fiber tip was initially positioned in contact with the phantom (Fig. 2(a)). A single Ho:YAG laser pulse

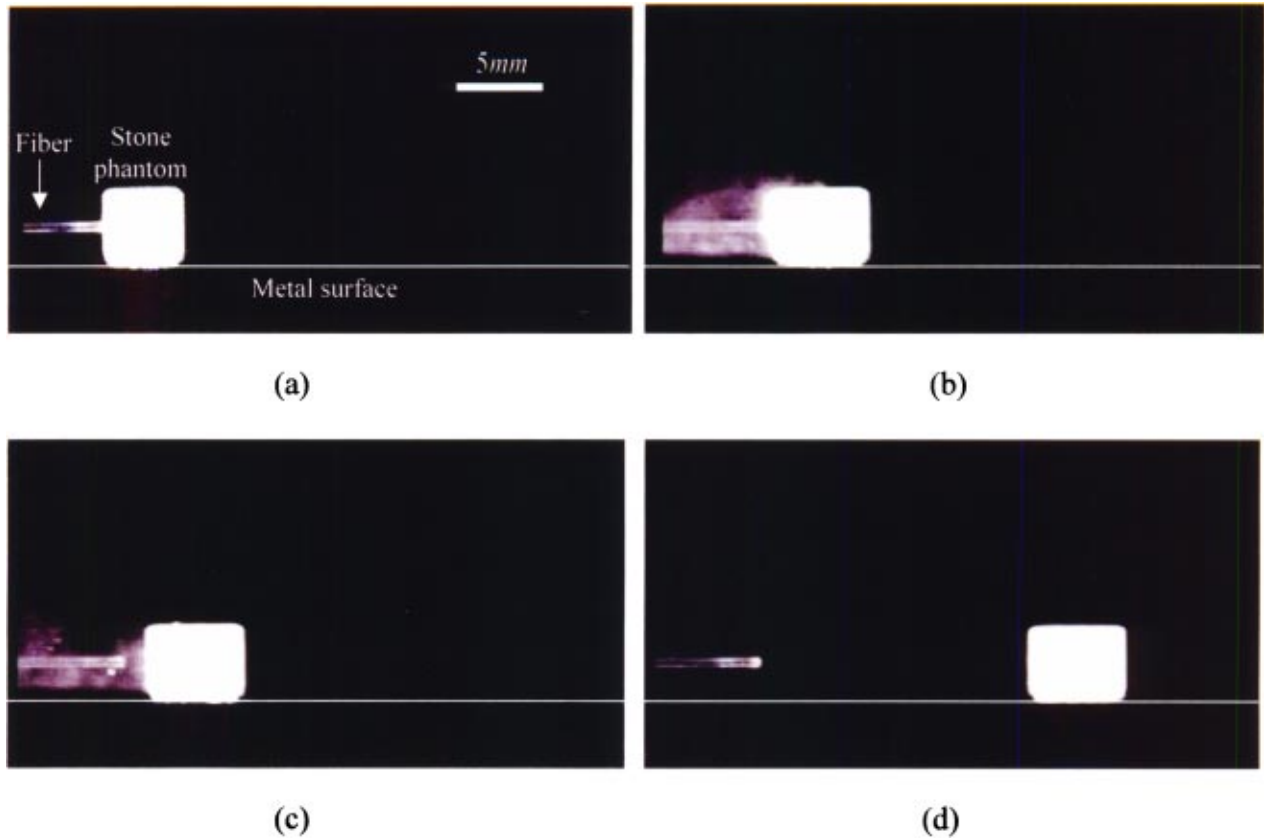


Fig. 2 Calculus phantom recoil after laser pulse (Fiber diameter=940 μm , incident laser energy=1 J and $H_0=144 \text{ J/cm}^2$). (a) before laser pulse, (b) 4 msec, (c) 8 msec, and (d) 60 msec after the onset of the pulse.

irradiated the phantom, and the ejected ablation plume (white particles) was observed around the fiber and the irradiated side (Fig. 2(b)). Due to the conservation of momentum, momentum imparted to the ejected particles created a recoil momentum on the phantom and the phantom moved away from the fiber (Fig. 2(c)). The phantom continued to move until friction and drag forces brought it to a new stationary position (Fig. 2(d)).

Recoil Momentum Dependence on the Fiber Size and Radiant Exposure, in Air. Figure 3 shows the recoil momentum (J_{rm}) of the phantom, surrounded by air in the glass tube, as a

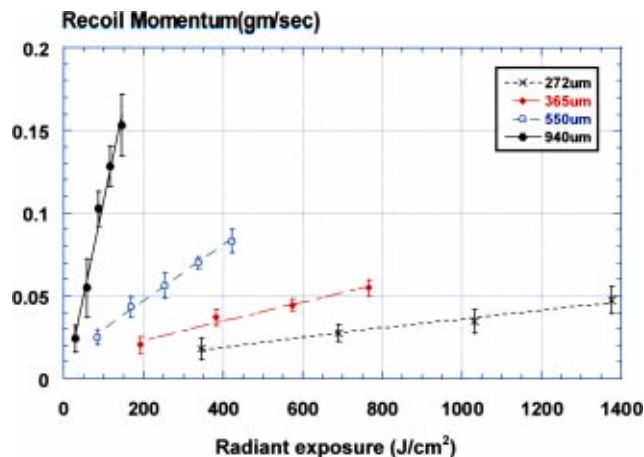


Fig. 3 Recoil momentum of 150 mg calculus phantoms as a function of Ho:YAG laser radiant exposure for different fiber diameters. Measurements were made in air.

function of radiant exposure (H_0) for four different fiber diameters. The radiant exposure (H_0) is defined as the incident laser pulse energy per unit area. Error bars represent the standard deviations. Recoil momentum was calculated using Eq. (1) and assuming the single laser pulse did not significantly decrease the initial 150 mg mass of the phantoms. The recoil momentum increased with radiant exposure for all four fiber sizes. For a given radiant exposure, the recoil momentum decreased with decreasing fiber diameter.

Calculus Phantom Recoil in Water. Figure 4 displays recoil momentum calculated from initial velocity of the phantom in water as a function of radiant exposure for four different fiber diameters. At the lowest two radiant exposure of each fiber, the recoil of the phantom was unidirectional (moving away from the fiber tip), similar to the recoil seen under the dry condition. However, at higher radiant exposure levels, the motions of the phantom deviated from those observed under the dry condition. At these radiant exposures, the laser pulse caused the phantom to move away initially. The top of the phantom then rocked back towards the fiber, while the phantom continued to move away from the fiber (Fig. 5). This data was not plotted in Fig. 4 because the initial velocity was affected by the nonlinear motion of the phantom.

Laser Induced Bubble and Re-entrance Flow. Figure 6 provides the sequence of the formation and collapse of the laser-induced bubble and the resulting re-entrance flow. In order to clearly visualize the dynamics of the rocking, a gap was introduced between the fiber and the phantom. This minimized the recoil motion and ensured that the rocking motion was the dominant movement. Suspended particles (pre-existing ablated debris from previously irradiated phantoms which appears as white dots in the pictures) were introduced in the water in order to visualize the current of the re-entrance flow. The exposure time of the cam-

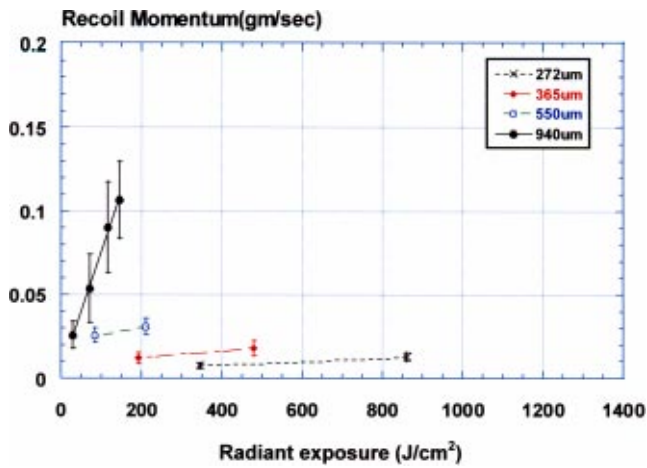
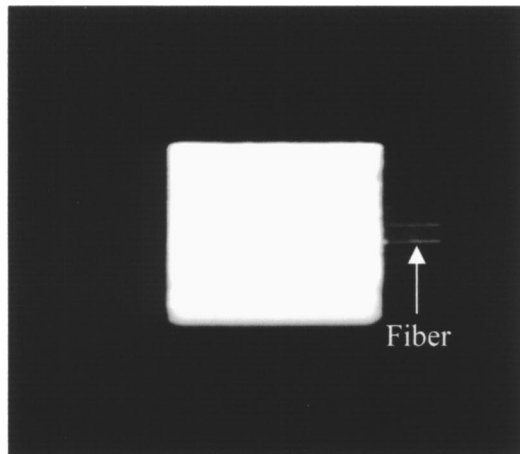


Fig. 4 Recoil momentum of 150 mg calculus phantoms as a function of Ho:YAG laser radiant exposure for different fiber diameters. Measurements were made in water.

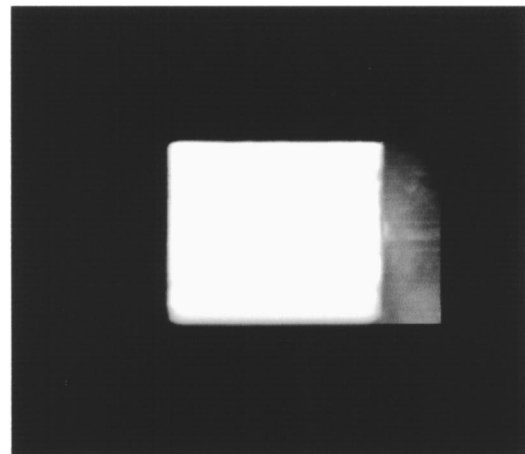
era was set at 4 msec. Before the pulse, the phantom was at rest in the glass tube (Fig. 6(a)) and a bubble was created by the pulse (Fig. 6(b)). The collapse of the bubble created the re-entrance flow which can be observed as the tail of the suspended particle (Fig. 6(b) and (c)). The re-entrance flow caused the stone to rock towards the fiber (Fig. 6(c)), after which, the stone fell back to the resting position (Fig. 6(d)).

Laser-Induced Crater Topography. After exposure to a single Ho:YAG laser pulse, ablation craters were scanned with an OCT instrument and the cross sectional profiles are displayed in Fig. 7. Typical images for the largest (940 μm) and smallest (273 μm) fiber diameters are shown. An increase in laser energy produced larger craters for all four fibers. The crater shape was also affected by fiber size. At a given laser energy, irradiation with the larger fiber produced wider and shallower craters.

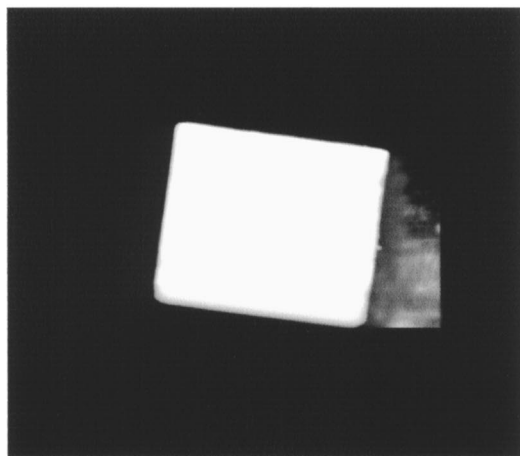
Ablation Volume as a Function of the Fiber Size and Radiant Exposure. The ablation volumes, calculated from cross-sectional OCT image, are provided in Fig. 8. Error bars indicate the standard deviation of the measurement. Use of higher radiant exposure produced a larger ablation volume for any fiber diameter.



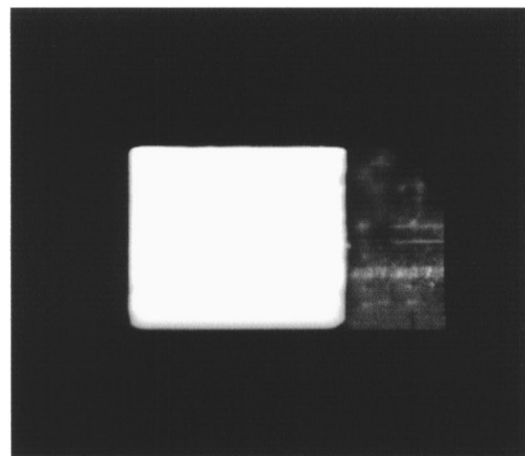
(a) Before the pulse



(b) 2msec after the pulse



(c) 6msec after the pulse



(d) 20msec after the pulse

Fig. 5 Rocking of phantom in water after pulse (Fiber diameter=550 μm , input laser energy=600 mJ, and $H_0 = 252 \text{ J/cm}^2$).

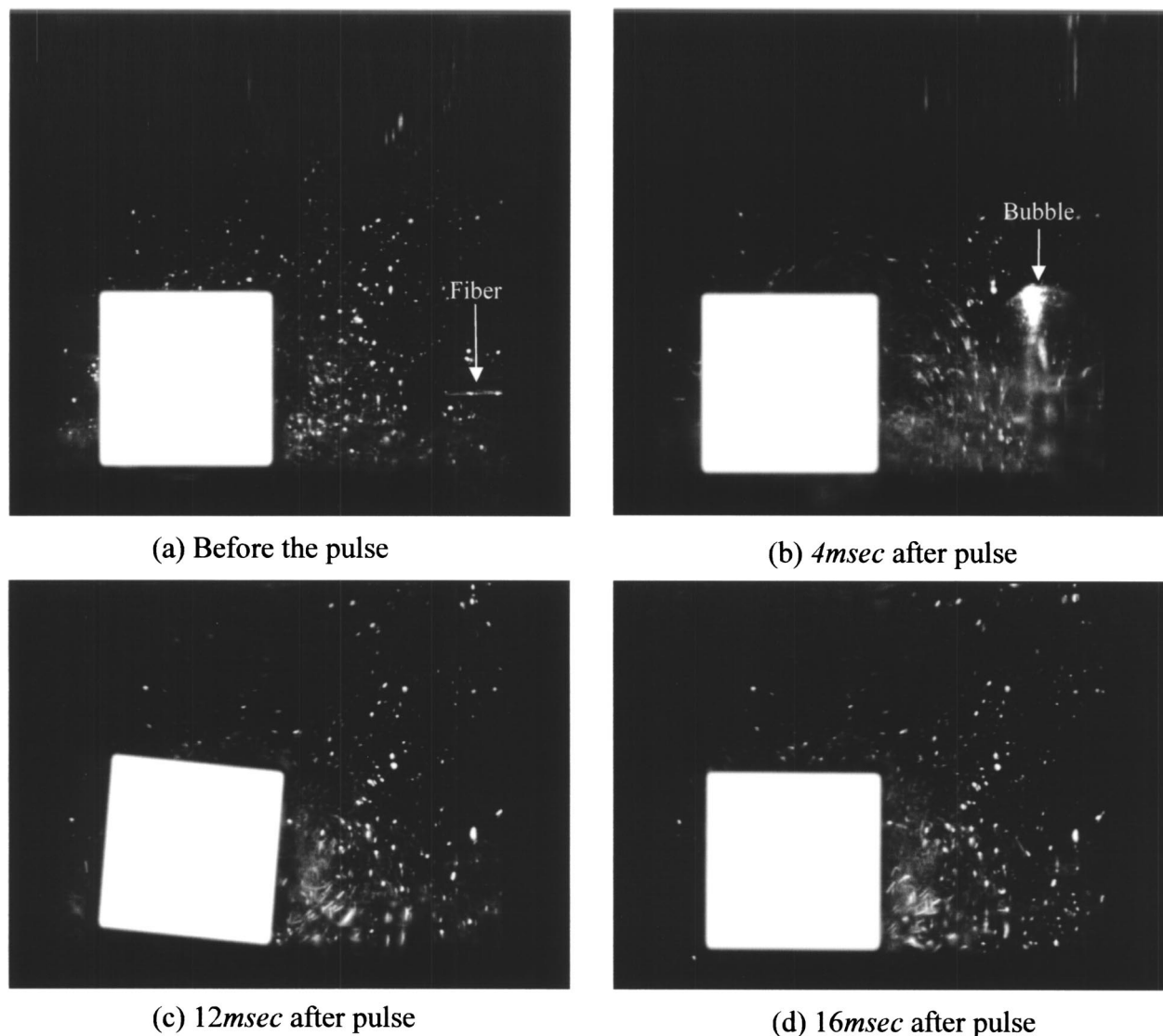


Fig. 6 Laser-induced bubble and re-entrance flow (Fiber diameter=550 μm , input laser energy=600 mJ, and $H_0 = 252 \text{ J/cm}^2$).

Propagation of Ejected Particles. Figure 9 consists of three series of images that shows the propagation direction of the ablated plume during laser ablation of burn paper. Even when the target (burn paper) is at an angle with respect to the laser beam, the ejected plume propagates in the direction normal to the burn paper surface.

Discussion

During lithotripsy, recoil of a calculus is the result of a number of interrelated phenomena. First, a minute pressure (termed “radiation pressure”) is exerted on a target surface due to the momentum transfer from photon to target. This momentum transfer takes place as a result of photon energy absorption regardless of the occurrence of ablation [11,24]. Since the magnitude of the radiation pressure is much smaller than ablation-induced recoil stress (pressure), it was neglected. At super-ablation radiant exposure, the ejection of the ablated plume causes the calculus to recoil away from the fiber to conserve momentum [8–11]. The ejection velocity, total mass, and the propagation direction of the ejected plume determine the recoil momentum. If the pressure of the ex-

panding vapor is higher than the ambient pressure, an additional force (the product of the pressure difference and irradiation area) causes the calculus to recoil.

Many previous studies have proposed analytical solutions for recoil momentum based on two distinct ablation models [25]. Phipps et al., and Venugopalan et al. proposed an “explosive ablation” process, in which the entire laser pulse energy is absorbed prior to the onset of material ejection [19,26]. According to this model, a portion of the laser pulse provides the heat of ablation (which is the energy required to initiate ablation) and the remainder of the absorbed pulse is kinetic energy of the ablated plume that determines the amplitude of the recoil momentum. This model is suitable for Q-switched IR laser-induced ablation process, in which the pulse duration ($\tau_p < 1 \mu\text{sec}$) is short enough to satisfy the assumption that all of the pulse energy is absorbed prior to ablation.

The “steady-state vaporization” model is more appropriate for interpreting the recoil momentum induced by a continuous laser or long pulsed laser [15–18]. This model was first proposed to describe the ablation of metal and UV laser-induced ablation. The schematic diagram in Fig. 10 describes the material ablation driven by a continuous vaporization process. Laser-induced vapor

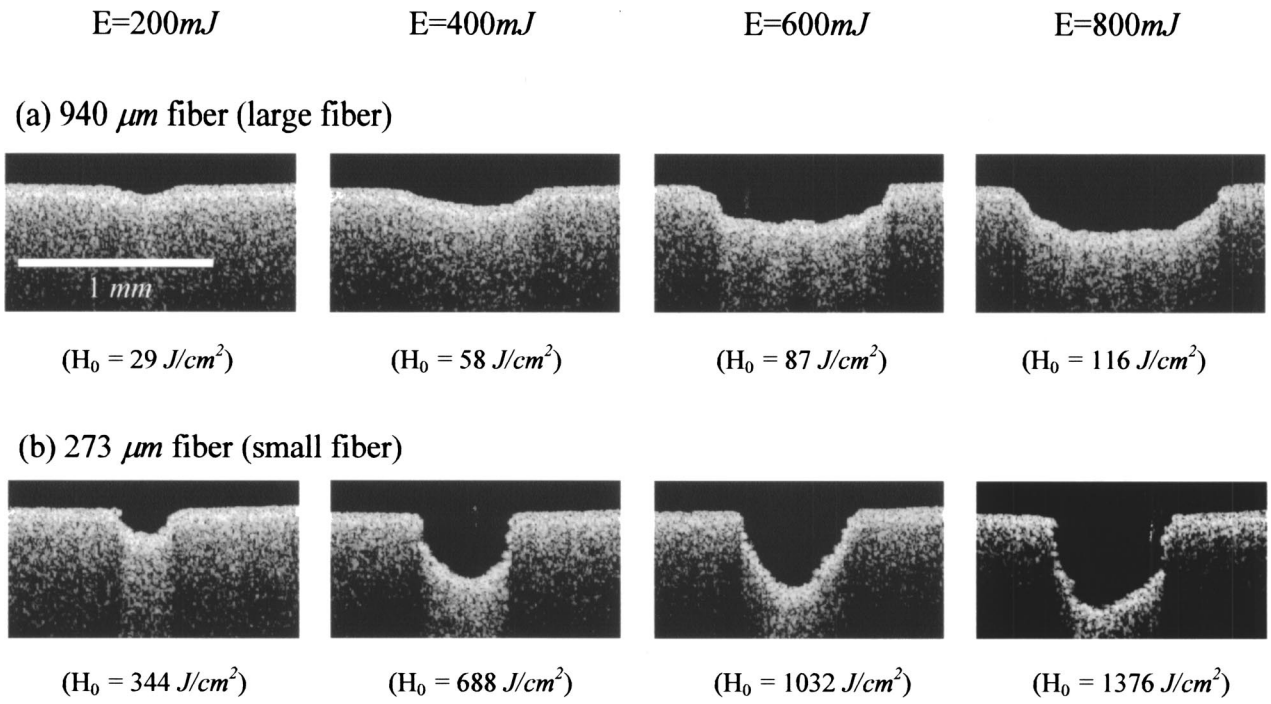


Fig. 7 Cross-sectional topography of Ho:YAG laser-induced craters acquired with OCT.

moves away from the ablation front with a velocity v . In order to conserve the momentum, a recoil stress (recoil pressure) p_0 is exerted on the surface.

$$p_0 = p_1 + \dot{m}v \quad (2)$$

where p_1 is the pressure of expanding vapor, \dot{m} is the ejected mass rate per unit area, and $\dot{m}v$ represents the momentum rate carried out by vapor flow per unit area. The recoil stress (p_0) is based on gas-dynamic equations: the continuity equation, the Navier-Stokes equation, and the equation of energy conservation. The estimated vapor pressure, the momentum rate of the vapor flow, and recoil stress almost linearly increase with the laser radiant exposure over the range used in this study [17,18].

$$p_1 = c_1 H_0 \quad (3)$$

$$\dot{m}v = c_2 H_0 \quad (4)$$

$$p_0 = (c_1 + c_2) H_0 \quad (5)$$

where c_1 and c_2 are constants of proportionality. Details of the derivation process may be found in Refs. [17] and [18]. The linear dependency of recoil stress on the laser radiant exposure has been observed in previous studies [13,14,17]. From Eq. (5), the resultant force and recoil momentum are given by the expression:

$$F = p_0 A = (c_1 + c_2) H_0 A \quad (6)$$

$$J = \tau_p F = \tau_p (c_1 + c_2) H_0 A \quad (7)$$

where F is the force that recoils the target, A is the irradiation area and τ_p is the pulse duration. The recoil momentum can be divided into two terms as follows:

$$J = J_1 + J_2 \quad (8)$$

$$J_1 = \tau_p c_1 H_0 A = \tau_p p_1 A \quad (9)$$

$$J_2 = \tau_p c_2 H_0 A = \sum_i m_i v_i \quad (10)$$

where m_i is the mass of ablated particles and v_i is the velocity along the laser-incident axis. J_1 and J_2 represent the recoil momentum induced by the pressure difference and the ejection of the mass, respectively.

The measured recoil momentum increases linearly with increasing laser radiant exposure as indicated by Eq. (7). This result is not surprising because higher radiant exposure typically result in a larger ablation mass, increasing the recoil momentum of the phantom.

Eq. (7) also suggests that the recoil momentum is proportional to the irradiation area as well as the radiant exposure. To investigate the dependency of recoil momentum on fiber diameter, the measured recoil momentums were linearly curve-fitted using a least-square method. The ratios between slopes of each fiber are compared along with the ratio between the irradiation areas in Fig. 11. According to Eq. (7), the ratios between slopes of recoil momentum should be identical to the ratios of irradiation area. How-

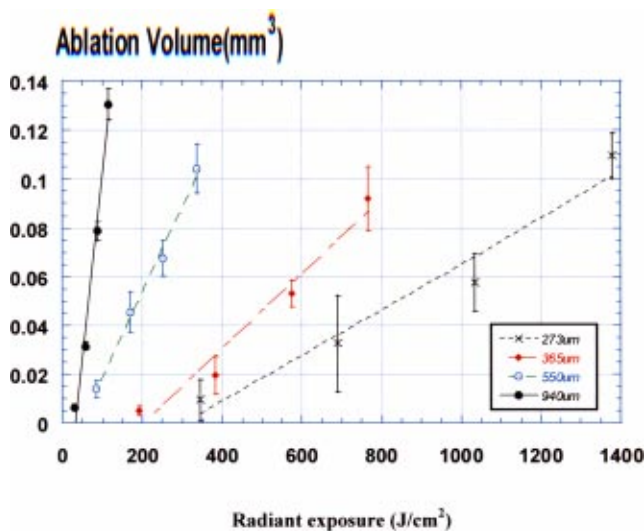
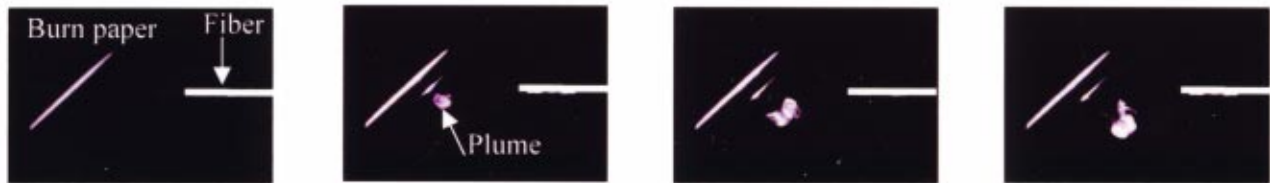


Fig. 8 Ablation volumes as a function of laser radiant exposure and fiber diameter. Measurements were made in air.

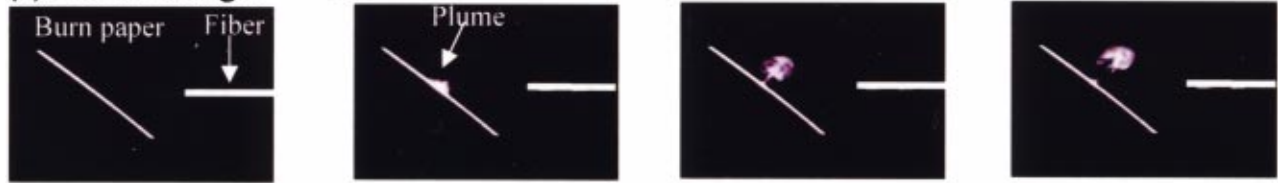
(a) Incident angle = 90°



(b) Incident angle = +45°



(c) Incident angle = -45°



Before pulse

T=2msec

T=4msec

T=6msec

Fig. 9 Direction of plume propagation with different incident angles (Fiber diameter=940 μm, input laser energy=500 mJ and $H_0=72.5 \text{ J/cm}^2$).

ever, as shown in Fig. 11, the ratios between slopes are lower than the values expected from the area ratios. This implies that the decrease of recoil momentum by a smaller fiber cannot solely be explained by the smaller irradiation area.

In order to account for the reduction of recoil momentum by a smaller fiber, we proposed a mechanism based on the plume propagation direction and crater shape. The estimated recoil momentums in Eq. (7) is valid under the condition that the ablation front (laser-induced crater) over the whole laser spot is normal to the laser-incident axis, as depicted in Fig. 10. J_1 (the product of vapor pressure and irradiating area) is independent of the crater geometry; however J_2 needs to be modified when the ablation front (laser-induced crater) is contoured (i.e., it has a certain angle with respect to the laser-incident axis) as observed in OCT images in Fig. 7. If ablated materials (of total mass m_t) escape with a

velocity v and the propagation direction is parallel with the laser-incident axis (Fig. 10), J_2 is simply expressed as:

$$J_{2,n} = m_t v \quad (11)$$

If the ablated material propagates with a certain angle with respect to the laser-incident axis, only a portion of the velocity vectors contribute to the recoil momentum along the laser-incident axis

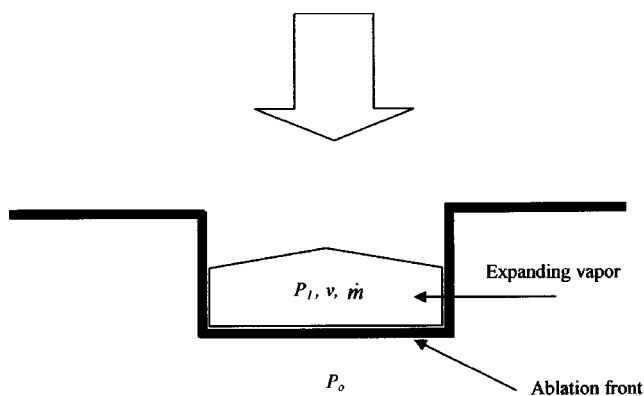


Fig. 10 Schematic representation of material ablation driven by a continuous ablation process.

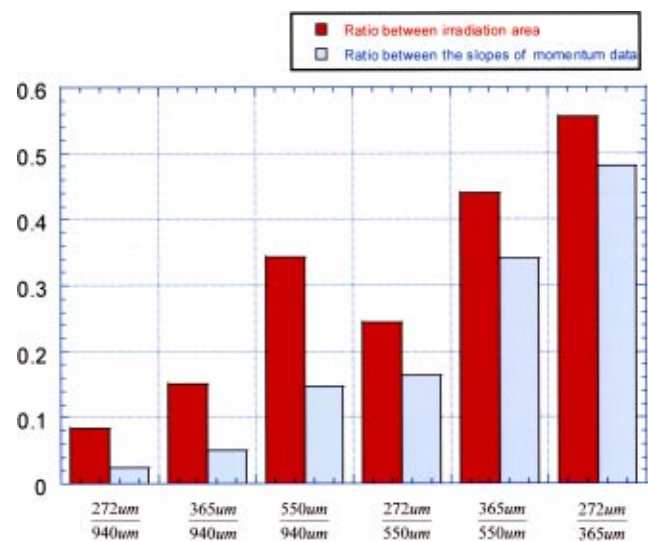


Fig. 11 Ratios between irradiation areas and ratios between the slopes of curve-fit lines of recoil momentum data.

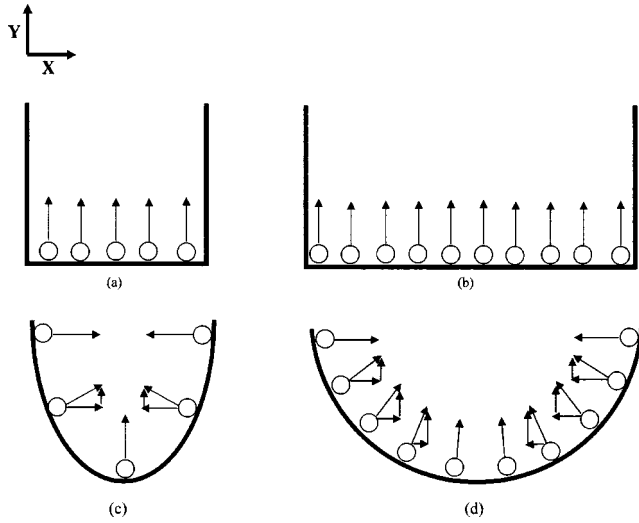


Fig. 12 Ejection of ablated particles from four distinct craters. Velocity vectors are resolved into X and Y components.

and the resultant recoil momentum should be smaller than $J_{2,n}$. In order to quantify the diminution of J_2 due to the crater contour, we defined the diminution factor as follows:

$$\alpha = \frac{J_{2,n}}{J_{2,c}}, \quad 0 < \alpha < 1 \quad (12)$$

where $J_{2,c}$ is the recoil momentum by material ejection on a contoured ablation front. For a given radiant exposure, a smaller fiber produces narrow craters with a steep contoured geometry due to its smaller irradiation area compared to a larger fiber [23]. This trend is confirmed by OCT images (Fig. 7) revealing that the crater curvature increases as the fiber diameter decreases. Figure 12 shows an illustration that demonstrates how the differences in crater topography affect recoil momentum. Crater (a) and (b) have a flat bottom and craters (c) and (d) have a contoured bottom. The irradiation area (A_2) of craters (b) and (d) are set to be twice the irradiation area (A_1) of crater (a) and (c). For example, consider that five ablated particles for crater (a) and (c) and ten particles for crater (b) and (d) were produced at a certain time; the number of ablated particles (ablation mass) was assumed proportional to the irradiation area for a give radiant exposure. Laser-induced particles will be ejected in a direction normal to the surface (that is confirmed by the plume propagation experiment, Fig. 9). The particles will generate a force on the calculus in the opposite direction of their propagation. The velocity of particles can be divided into two components (x and y axis). The x components of particles cancel each other and hence do not contribute to the recoil momentum. Only the y components will make the calculus move in the negative y direction (along the laser-incident axis). In the case of crater (a) and (b), since the velocity of ejected particles does not have x component, the recoil momentum induced by the ejection of particles is expressed from Eq. (10) as follows:

$$\text{Crater (a): } J_{2,a} = \tau_p c_2 H_o A_1 \quad (13)$$

$$\text{Crater (b): } J_{2,b} = \tau_p c_2 H_o A_2 \quad (14)$$

And the ratio between $J_{2,n,a}$ and $J_{2,n,b}$ is determined by the ratio of areas as follows:

$$\frac{J_{2,a}}{J_{2,b}} = \frac{\tau_p c_2 H_o A_1}{\tau_p c_2 H_o A_2} = \frac{A_1}{A_2} \quad (15)$$

Regarding craters with contoured ablation fronts, the recoil momentum induced by the ejection of particles is expressed as follows:

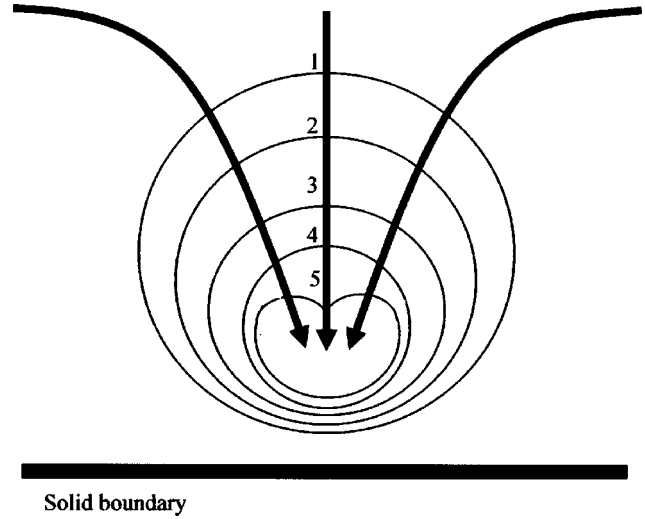


Fig. 13 Asymmetric bubble collapse near a solid boundary. Numbers indicate time sequence of the bubble collapse which is on the order of 100 μ sec.

$$\text{Crater (c): } J_{2,c} = \alpha_c J_{2,a} = \alpha_c \tau_p c_2 H_o A_1 \quad (16)$$

$$\text{Crater (d): } J_{2,d} = \alpha_d J_{2,b} = \alpha_d \tau_p c_2 H_o A_2 \quad (17)$$

where α_c and α_d are the diminution factors of contoured craters (c) and (d), respectively. Then, the ratio between $J_{2,c}$ and $J_{2,d}$ is determined not only by the ratio of areas but also by the ratio between the diminution facts as following:

$$\frac{J_{2,c}}{J_{2,d}} = \frac{\alpha_c \tau_p c_2 H_o A_1}{\alpha_d \tau_p c_2 H_o A_2} = \frac{\alpha_c A_1}{\alpha_d A_2} \quad (18)$$

The diminution factor α is governed by the contour of the ablation front; the steeper the contour is, the greater α is. Accordingly, the ratio $J_{2,c}/J_{2,d} = \alpha_c A_1 / \alpha_d A_2$ is smaller than $J_{2,a}/J_{2,b} = A_1 / A_2$ since α_c is smaller than α_d . This can explain why a smaller fiber, which creates a more rounded crater, produces a recoil momentum smaller than the value that is expected from the ratio between irradiation areas.

In the presence of water, we observed the phantom rocking after the laser pulse (Fig. 5). Absorption of a small portion of the Ho:YAG pulse energy in water produces a bubble. The re-entrance flow of water induced by the bubble collapse (Fig. 6) is considered to be the cause of the rocking of the phantom. During lithotripsy, the surrounding water is a highly absorbing medium for the Ho:YAG laser beam. Once the water absorbs the laser pulse energy, the water is vaporized, forming a bubble, and the bubble eventually collapses. If there is no solid boundary near the bubble, the bubble collapses symmetrically. If a solid boundary exists near the bubble, the bubble will collapse asymmetrically due to retarded flow near the solid boundary [27–32]. Figure 13 demonstrates the asymmetric bubble collapse process near a solid boundary. Numbers in the Fig. 13 indicate the time sequence (Number 1 indicates the initial stage of bubble collapse and number 5 indicates the last stage of collapse). As the bubble collapses, the upper boundary deforms more rapidly than the lower boundary, this is because the re-entrance flow from the bottom of the bubble is retarded by the viscous force due to the presence of the solid boundary. As a consequence, the bubble collapses asymmetrically which results in a powerful microjet flow (represented by arrows) that may lead to physical damage on the solid surface [30].

Based on the microjet phenomenon, the rocking after the pulse can be explained by the following mechanism. 1) The calculus phantom is at rest before the pulse (Fig. 14(a)). 2) The laser pulse produces an ablation plume, recoil motion is initiated, and a water bubble is formed (Fig. 14(b)). 3) The water bubble collapses

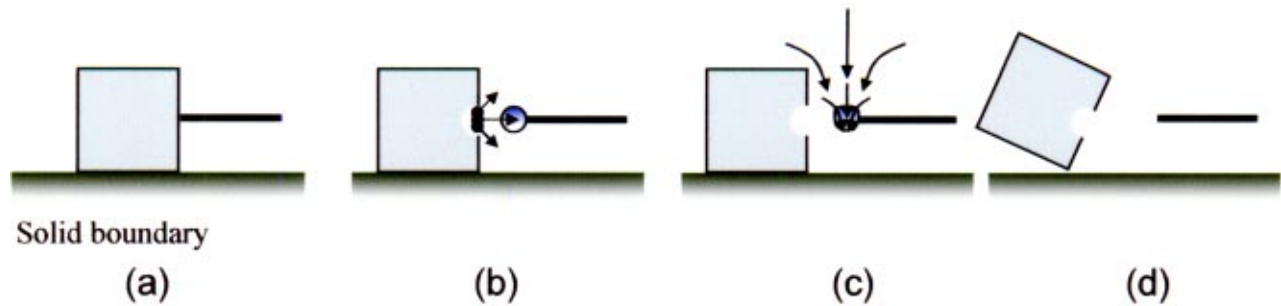


Fig. 14 Proposed mechanism of calculus rocking.

asymmetrically due to the presence of the solid boundary, which results in a re-entrance flow from the top to the bottom (Fig. 14(c)). 4) The re-entrance flow causes the top of phantom to rock (Fig. 14(d)).

Based on our observations: we suggest 1) using small diameter fibers to minimize retropulsion during Ho:YAG lithotripsy and 2) using the laser at modest radiant exposures (energy levels) to minimize the effect of re-entrance flow as well as retropulsion.

Conclusion

We quantified the recoil momentum of calculus phantom during the Ho:YAG laser lithotripsy. The dependency of recoil on the fiber size and laser radiant exposure was determined. The correlation among crater shape, debris trajectory and recoil momentum was investigated. Higher laser radiant exposure resulted in larger ablation volume (mass) which increased the recoil momentum. The smallest fiber produced a more rounded crater and diminished recoil momentum compared to the largest fiber. The shape of the crater was one of the major contributing factors to the augmented recoil momentum of larger fibers. In the presence of water, recoil motion of the stones deviated from that of stone in air. Under certain conditions, bubble was formed and calculus rocking was observed after the laser pulse. The re-entrance flow of water induced by the bubble collapse was postulated as the cause of the rocking of the calculus.

In the clinic, the retropulsion of calculus is erratic 3-D. However, the most problematic displacement is along the fiber axis (laser axis), since the lateral movement of calculus is limited by the wall of ureter. Physicians describe this type of axial retropulsion of calculus as the “playing pool” the calculus is shoot by light from the fiber as a cue tip hits a ball on a pool table. This study is designed to investigate the retropulsion of calculus along the fiber axis (laser-incident axis). To minimize retropulsion during Ho:YAG lithotripsy, we suggest using small diameter fibers at modest radiant exposure levels.

Acknowledgments

Funding for this research was provided by the Albert W. and Clemmie A. Caster Foundation. The authors would like to thank Lumenis Inc. for providing their laser. We also appreciate Professor David T. Blackstock of the Department of Mechanical Engineering, the University of Texas at Austin, for his valuable advice on the physics of bubble dynamics.

Nomenclature

J	= linear recoil momentum, $\text{kg} \times \text{m}/\text{sec}$
m	= mass, kg
v	= initial velocity, m/sec
$\Delta\lambda$	= bandwidth, nm
λ_0	= wavelength, nm
OCT	= optical coherence tomography
H_0	= radiant exposure, J/cm^2

p_0	= recoil stress (recoil pressure), N/m^2
p_1	= pressure of expanding vapor, N/m^2
\dot{m}	= ejected mass rate per unit area, $\text{kg}/(\text{sec} \times \text{m}^2)$
F	= recoil force, N
A	= irradiation area, m^2
τ_p	= pulse duration, sec
α	= diminution factor

References

- [1] Dretler, S. P., 1988, “Laser lithotripsy: A review of 20 years of research and clinical applications,” *Lasers Surg. Med.*, **8**, pp. 341–356.
- [2] Chan, K. F., Pfefer, T. J., Teichman, J. M. H., and Welch, A. J., 2001, “A perspective on laser lithotripsy: The fragmentation process,” *J. Endourol.*, **15**, pp. 257–273.
- [3] Watson, G., Murray, S., Dretler, S. P., and Parrish, J. A., 1987, “The pulsed dye laser for fragmenting urinary calculi,” *Journal of Urology*, **138**, pp. 195–198.
- [4] Denstedt, J. D., Chun, S. S., Miller, M. D., and Eberwein, P. M., 1997, “Intracorporeal lithotripsy with the Alexandrite laser,” *Lasers Surg. Med.*, **20**, pp. 433–436.
- [5] Chan, K. F., Vassar, G. J., Pfefer, T. J., Teichman, J. M. H., Glickman, R. D., Weintraub, S. T., and Welch, A. J., 1999, “Holmium:YAG Laser Lithotripsy: A dominant photothermal ablative mechanism with chemical decomposition of Urinary Calculi,” *Lasers Surg. Med.*, **25**, No. 1, pp. 22–37.
- [6] Hofmann, R., Hartung, R., Geissdorfer, K., Ascherl, R., Erhardt, W., Schmidt-Kloiber, H., and Reichel, E., 1988, “Laser induced shock wave lithotripsy-biologic effects of nanosecond pulses,” *Journal of Urology*, **139**, pp. 1077–1079.
- [7] Rink, K., Delacretaz, G., and Salathe, R. P., 1995, “Fragmentation process of current laser lithotriptors,” *Lasers Surg. Med.*, **16**, pp. 134–146.
- [8] Frenz, M., Zweig, A. D., Romano, V., and Weber, H. P., 1990, “Dynamics in laser cutting of soft media,” *Proceeding of SPIE*, **1202**, pp. 22–33.
- [9] Kuznetsov, L. I., 1993, “Recoil momentum at a solid surface during developed laser ablation,” *Quantum Electron*, **23**, No. 12, pp. 1035–1038.
- [10] White, M. D., Moran, M. E., Calvano, C. J., Borhan-Manesh, A., and Mehlhaff, B. A., 1998, “Evaluation of retropulsion caused by holmium:YAG laser with various power settings and fibers,” *J. Endourol.*, **12**, No. 2, pp. 183–186.
- [11] Foth, H. J., Meyer, D., and Stöckel, T., 2000, “Side effects of laser tissue interaction studied by laser Doppler vibrometry,” *Proceeding of SPIE*, **4072**, pp. 392–400.
- [12] Kuznetsov, L. I., 1995, “Energy balance of interaction pulse laser radiation with a target,” *Proceeding of SPIE*, **2376**, pp. 269–277.
- [13] Hibst, R., 1992, “Mechanical effects of Erbium:YAG laser bone ablation,” *Lasers Surg. Med.*, **12**, pp. 125–130.
- [14] Auerhammer, J. M., Walker, R., van der Meer, A. F. G., and Jean, B., 1999, “Dynamics behavior of photoablation products of corneal tissue in the mid-IR: a study with FELIX,” *Applied Physics B*, **68**, pp. 111–119.
- [15] Anisimov, S. I., 1968, “Vaporization of metal absorbing laser radiation,” *Soviet Physics JETP*, **27**, pp. 182–183.
- [16] Zweig, A. D., 1991, “A thermo-mechanical model for laser ablation,” *J. Appl. Phys.*, **70**, pp. 1684–1691.
- [17] Cummings, J. P., and Walsh, Jr., J. T., 1993, “Tissue tearing caused by pulsed laser-induced ablation pressure,” *Appl. Opt.*, **32**, pp. 494–502.
- [18] Krokhn, O. N., 1972, “Laser Handbook,” Amsterdam: North-Holland, Vol. 2, pp. 1371–1384.
- [19] Venugopalan, V., Nishioka, N. S., and Mikic, B. B., 1996, “Thermodynamics response of soft biological tissues to pulsed infrared-laser irradiation,” *Biophys. J.*, **70**, pp. 2981–2993.
- [20] Huang, D., Swanson, E. A., Lin, C. P., Schuman, J. S., Stinson, W. G., Chang, W., Hee, M. R., Flotte, T., Gregory, K., Puliafito, C. A., and Fujimoto, J. G., 1991, “Optical coherence tomography,” *Science*, **254**, pp. 1178–1181.
- [21] Izatt, J. A., Kulkarni, M. D., Yazdanfar, S., Barton, J. K., and Welch, A. J., 1997, “In vivo bidirectional color Doppler flow imaging of picoliter blood

- volumes using optical coherence tomography." *Opt. Lett.*, **22**, pp. 1439–1441.
- [22] Barton, J. K., Welch, A. J., and Izatt, J. A., 1998, "Investigating pulsed dye laser-blood vessel interaction with color Doppler optical coherence tomography," *Opt. Express*, (<http://www.opticsexpress.org/>), **3**, No. 6, pp. 251–256.
- [23] Ostertag, M., McKinley, J. T., Reinisch, L., Harris, D. M., and Tolk, N. H., 1997, "Laser ablation as a function of the primary absorber in dentin," *Lasers Surg. Med.*, **21**, pp. 384–394.
- [24] Hecht, E., 1998, "Optics," New York: Addison Wesley Longman Inc., 3rd, pp. 55–57.
- [25] Vogel, A., and Venugopalan, V., 2003, "Mechanisms of pulsed laser ablation of biological tissues," *Chemical Reviews*, **103**, pp. 577–644.
- [26] Phipps, Jr., C. R., Harrison, R. F., Shimada, T., York, G. W., Turner, T. P., Corlis, X. F., Steele, H. S., Haynes, L. C., and King, T. R., 1990, "Enhanced vacuum laser-impulse coupling by volume absorption at infrared wavelength," *Laser Part. Beams*, **8**, pp. 281–297.
- [27] Plesset, M. S., and Chapman, R. B., 1971, "Collapse of an initially spherical vapor cavity in the neighborhood of a solid boundary," *J. Fluid Mech.*, **47**, pp. 283–290.
- [28] Lauterborn, W., and Bolle, H., 1975, "Experimental investigations of cavitation bubble collapse in the neighborhood of a solid boundary," *J. Fluid Mech.*, **72**, pp. 391–399.
- [29] Tomita, Y., and Shima, A., 1990, "High-speed photographic observations of laser-induced cavitation bubbles in water," *Acustica*, **71**, pp. 161–171.
- [30] Brennen, C. E., 1995, "Cavitation and Bubble Dynamics," New York: Oxford University Press, pp. 78–83.
- [31] Niemi, M. H., 1996, "Laser-Tissue Interactions," Berlin: Springer, pp.145–147.
- [32] Vogel, A., Lauterborn, V., and Timm, R., 1989, "Optical and acoustical investigation of the dynamics of laser-produced cavitation bubbles near a solid boundary," *J. Fluid Mech.*, **206**, pp. 299–228.